Microstructure and texture characterization in friction stir lap welded TIMETAL 21S

Thierry Baudin, François Brisset, Anatoliy Zavdoveev, Hiba Azzeddine

Microstructure and texture characterization in friction stir lap welded TIMETAL 21S

Thierry Baudin[1], François Brisset[1], Anatoliy Zavdoveev[2], Hiba Azzeddine[3]*

[1] Université Paris-Saclay, CNRS, Institut de chimie moléculaire et des matériaux d'Orsay, 91405, Orsay, France.

[2] Paton Electric Welding Institute of NAS of Ukraine, Bozhenko N. 11, 03680 Kiev, Ukraine.

[3] Laboratory of Materials and Renewable Energy, Faculty of Sciences, Mohamed Boudiaf University, 28000, M'sila, Algeria.

* Corresponding author: Pr. Hiba Azzeddine, email: hiba.azzeddine@univ-msila.dz

Abstract

The evolution of microstructure and texture during friction stir lap welding (FSLW) of TIMETAL 21S (β-type Ti-15Mo-3Nb-3Al-0.2Si, wt.%) sheets were investigated through electron backscatter diffraction (EBSD). Excellent grain refinement is obtained through stir zone (SZ) thickness (1.2-1.8 µm). The microstructure of the thermomechanically affected zone (TMAZ) is characterized by elongated deformed grains surrounded by small recrystallized grains indicating the occurrence of discontinuous dynamic recrystallization (DDRX). The microstructure of heat affected zone (HAZ) is quite similar to the base metal (BM). The texture transformed from weak rolling-recrystallization texture in BM and HAZ to a typical shear texture with the domination of D_1 or D_2 components in the SZ and TMAZ area. A net shear texture gradient is formed across the SZ thickness which is connected with the heterogeneity of deformation. It is believed that the concomitant occurrence of grain size, dislocation and texture strengthening is responsible for the mechanical property distribution in different parts of FSLW joint.

Keywords: Friction stir welding; Microstructure; Texture; TIMETAL 21S; Titanium

1. Introduction

Friction-stir welding (FSW) is a well-known solid-state, hot-shear joining process using a non-consumable tool invented and patented by the welding institute (TWI) in 1991[1]. Nowadays, FSW is used in welding applications for a variety of metals and alloys with low melting temperature such as Aluminum [2, 3], and Magnesium [4] and also for high melting temperature like Iron [5] and Titanium [6]. The principle of FSW is very simple consisting of a tool, typically formed of a pin and shoulder, is rotated and plunged into two workpieces and then translated in a specific direction. The deformation and frictional heat induced by the rotating tool ensure the bonding between the two workpieces by the formation of a solid-state weld [7].

Different welding joint types can be produced by FSW such as butt joint, lap joint, edge joint, and T-joint depending on the way the pieces of metal are put together or aligned with each other [8]. The butt and lap joints welding are the most common type used in the sheet welding industry. In the butt joint, two pieces of metal are placed together in the same plane, and the side of each metal is joined by welding. While in the lap joint, the welding is produced on two pieces of metal placed on top of each other [8]. The friction stir lap welding (FSLW) is suitable for joining thin sheet structures [8].

Based on thermomechanical history, the cross-section of the welded material is usually separated into four zones, namely base metal (BM), thermomechanically affected zone (TMAZ), heat affected zone (HAZ), and stir zone (SZ) [7]. The SZ undergoes severe plastic deformation and high temperature after friction stir which assure the solid-state connection. TMAZ and HAZ are transition zones between the SZ and BM, in which the material is affected by a low amount of deformation and high temperature from the welding. Consequently, each zone exhibits a specific microstructural and textural evolution. Besides, the microstructure and texture are heterogeneously distributed through the SZ because of the effect of the FSW tool, on the strain and the temperature distribution across the SZ [9-12].

It must be noted that the inhomogeneous distribution of microstructure affects directly the mechanical properties of the weld. Nevertheless, FSW is considered as severe plastic deformation (SPD) processing that produces significant ultra-fine grains through dynamic recrystallization (DRX) [13]. The degree of grain refinement during FSW is strongly related to the deformation temperature and strain velocity [14-16]. Small grain size can be obtained through a combination of low deformation temperature and high strain rate [14-16].

Extensive investigations were performed during the last decade on FSW of α-type Ti alloys with hexagonal close-packed (HCP) crystal structure such as Ti-6Al-4V (wt.%) alloy [9, 10, 17-24]. Some studies were focused on the impact of FSW tool parameters such as the rotational and welding speed values on the microstructural evolution and the mechanical properties of the welded joints [9]. Other investigations focused on improving the superplasticity of the alloy through grain refinement induced by FSW [18, 20, 24].

Despite the suitable properties of β-Ti alloys having a single body-centered cubic (BCC) crystal structure in the aerospace and automobile industries or biomedical engineering [25-27], only limited investigations are available dealing with their microstructural and textural characterization after FSW [14, 28, 29]. In fact, the microstructure, texture and mechanical properties were investigated in detail for β-type Ti-15-3 alloy (Ti-15V-3Cr-3Al-3Sn, wt.%) after normal FSW and liquid CO_2 cooling FSW [28, 29]. But only a qualitative texture presentation as a function of welding speed was reported for β-type TIMETAL 21S alloy (Ti-15Mo-3Nb-3Al-0.2Si, wt.%) fabricated by FSW butt-joint [14].

Hence, the aim of the present study is the characterization in detail of the microstructure and texture evolution in different parts of a FSW joint (BM, HAZ, TMAZ, and SZ) of β-type TIMETAL 21S obtained by lap welding. It is believed that the present results help to elucidate the response of the present alloy to the FSW and extend our fundamental knowledge on the characteristic of FSW β-type Ti alloys.

2. Experimental procedure

The TIMETAL β-21S alloy was kindly received from TIMET Savoie, Ugine, France in the form of cold-rolled and subsequently annealed sheets with 1.6 mm of thickness. The chemical composition of the sheet TIMETAL β-21S alloy is given in Table 1. The alloy is produced with a single BCC structure that is supposed stable at room temperature. In addition, the precipitation of α-phase was not detected in similar TIMETAL β-21S alloy [14] and is not studied in the present work after welding.

Table 1. Chemical composition of TIMETAL β-21S alloy

Element	Mo	Nb	Al	Si	Fe	O	C	N	H	Ti
Weight %	14-16	2.4-3.2	2.5-3.5	0.15-0.25	0.4	0.11-0.17	0.05	0.05	0.015	Bal

Two sheets were superimposed and then lap welded by FSLW at the French Welding Institute (Institut de Soudure). The surface appearance of the 21S alloy weld joint is shown in Figure 1. The welding reference frame is welding direction (WD), transverse direction (TD), and

normal direction (ND). In the present case, the rolling direction (RD) is parallel to WD. The advancing side (AS) and retreating side (RS) are also indicated in the Figure.

The tool geometry was quite simple but confidential details were not given by the welding center. The welding was realized with welding speed of 50 mm/min with a constant tool rotation rate of 200 rpm. Argon shielding was used to avoid any oxidation of the sample and welding tool. The selection of specific welding speed and tool rotation was selected based on the investigation reported by Reynoled et al. [14] indicating that the combination of 50 mm/min and 200 rpm results in good welding appearance. The conic pin diameter was about 5 mm at the surface of the stacked sheets and the shoulder diameter was 30 mm (see Figure 1). An excellent surface appearance with no defects can be noticed indicating that a defect-free 21S alloy weld joint was successfully fabricated by FSW using the present welding parameters.

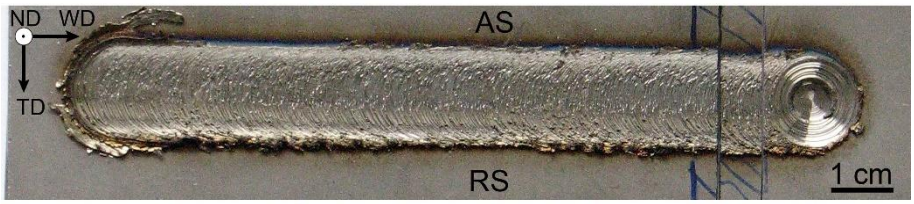

Figure 1: Photograph of the weld surface appearance. The welding reference frame are: welding direction (WD), transverse direction (TD), and normal direction (ND). Advancing side (AS), and retreating side (RS) are indicated.

The microstructure observations and texture analysis of the joints were carried out by EBSD measurements on the transverse cross-section (TD-ND plane) of the weld alloy.

Sample preparation consists of mechanical polishing using abrasive paper up to 2400 and then followed by a final polishing in 50 % colloidal silica (OP-S) + 49 % H_2O + 1% H_2O_2 solution in vibratory polisher for 17 h.

The EBSD measurements were carried out using a TSL-EDAX-Hikari system mounted on a scanning electron microscope FEG-SEM ZEISS Supra 55 VP operating at 20 kV. The data acquisition and analysis were processed by the Orientation Imaging Microscopy, OIM^{TM} software.

To manage these EBSD acquisitions, a batch including combo scans (beam control) and single scans (motor control) was programed. So, a scan area of about 16 × 4 mm^2 with a step size of 2 µm was firstly recorded using the combo function to get a general overview of the

FSLW microstructure. Then, several single scans and combo scans were analyzed with step size of 0.2 or 0.4 µm to analyze more precisely different parts of the FSLW joint.

For this study, the system was run continuously during 9 days without any user operation, showing the very good stability of the present SEM-EBSD analytical system. During this long-time acquisition, about 100 million Kikuchi patterns were acquired (exactly 97 922 014 points). The majority of these points was used to describe the microstructure and the texture of the studied sample.

A grain dilation and grain CI standardization clean-up with a grain tolerance angle of 5° and a minimum grain size of 5 pixels were applied to improve the quality of EBSD raw data. Due to the orientation noise, spurious boundaries with misorientation angles $\theta < 2°$ were excluded from EBSD maps [29]. In addition, all datum points with a confidence index (CI) lower than 0.05 were excluded from the quantitative analyses, where CI quantifies the reliability of the indexed pattern [30]. The mean grain size was measured using the equivalent diameter approach.

The grain orientation spread (GOS) and Kernel Average Misorientation (KAM) approaches in OIM™ software were used for the identification of recrystallized grains and strain distribution (dislocation density), respectively [31, 32]. GOS is defined as the average deviation between the orientation of each point in the grain and the average orientation of the grain, where grains with GOS < 1° are considered fully recrystallized [31].

KAM is known as the average misorientation angle of a given point with all its neighbors belong to the same grain [33]. In the present case, the θ_{KAM} value was calculated from the mean misorientation angle between a given point and its 3^{th} neighbors excluding misorientations greater than 5°. Hence the dislocation density can be obtained following the equation [34]:

$$\rho = \frac{\alpha \theta_{KAM}}{ndb} \quad (1)$$

where α = 3 for mixture of tilt and twist boundary types [34], b = 0.28 nm is the Burgers vector [35], n is the nearest neighbor and d is the scan step size.

MTEX software was used to analyze the evolution of texture by calculating the orientation distribution function (ODF) using the harmonic method (L = 22), and a gaussian function with a half-width of 5° to model each orientation [36].

The texture strength can be calculated by the texture index, I, using the following equation [37]:

$$I = \frac{1}{8\pi^2} \int_G f^2(g) dg \quad (2)$$

where *f(g)* is the ODF value, *G* is the Euler space.

3. Results and discussion

3.1. Microstructure and texture of TIMETAL 21S before FSW (BM)

Figure 2 shows the orientation imaging micrography (OIM) in inverse pole figure (RD-IPF) map and GOS map of the as-received (BM) S21 alloy. The black line indicates high angle boundaries (HAGBs) with misorientation θ > 15°. The average grain size and the grain recrystallized fraction are shown in the upper side of the RD-IPF and GOS maps, respectively.

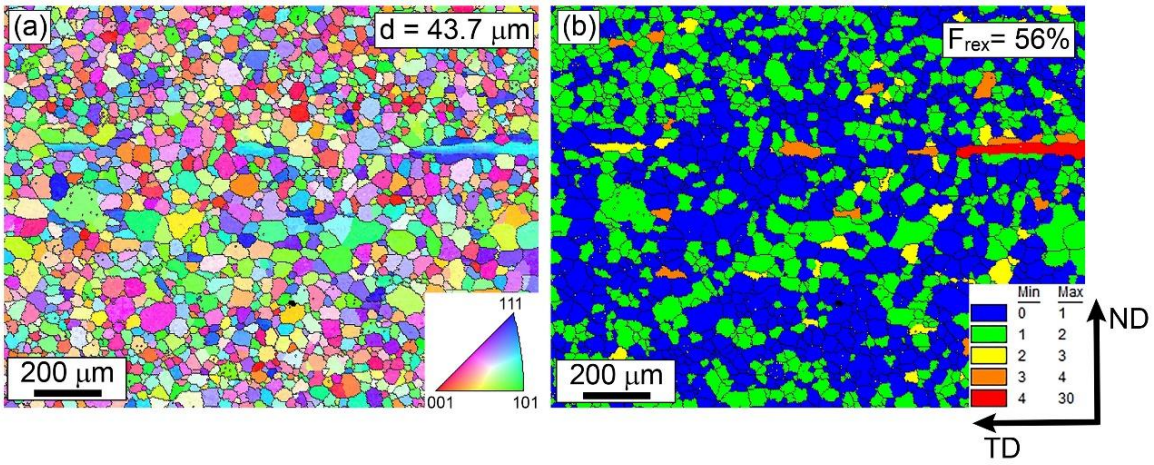

Figure 2: (a) RD-IPF and (b) GOS maps of the as-received (BM) 21S alloy.

The initial microstructure is characterized by equiaxed grains with mean grain size of about 43.7 µm and 54 % of grain boundaries are HAGBs type. The GOS map indicates that most of grains are recovered (green colour) and recrystallized (blue colour).

The initial texture of 21S alloy is shown in Figures 3a and c in term of the {110} pole figure and ODF section at $\varphi_2 = 45°$, respectively. The ideal deformation and recrystallization texture of rolled BCC alloys are shown for comparison in Figures 3b and d and their descriptions are given in Table 2. The texture of the as-received alloy is weak and characterized by the presence of deformed rolling texture components (A_1, A_2, B_2 and C_2) and recrystallized texture components (Cu and RCu).

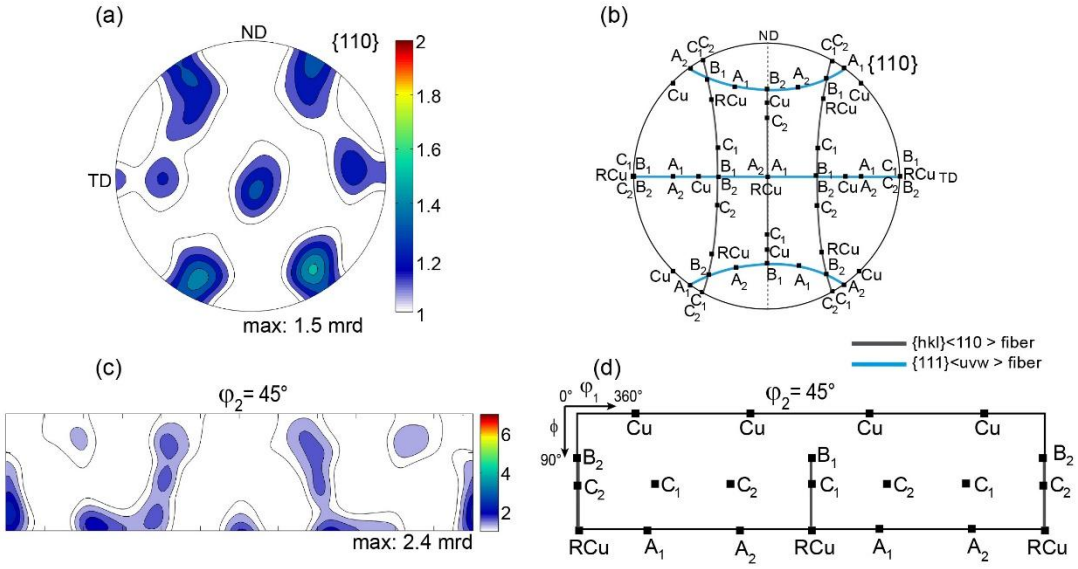

Figure 3: (a, c) {110} pole figure and ODF section at φ_2 = 45° of as-received (BM) 21S alloy and (b, d) main ideal texture component positions in {110} pole figure and ODF section at φ_2 = 45° of rolled BCC alloys.

Table 2. Position of ideal rolling texture components for BCC materials projected in TD-ND plane [38].

Notation	**TD-ND plane**	
Rolling component	Miller indice {hkl}<uvw>*	Euler angles (°) (φ_1, Φ, φ_2)
$\boldsymbol{A_1}$	{011} <$2\bar{1}1$>	(144.7, 45, 0)
$\boldsymbol{A_2}$	{011} <$21\bar{1}$>	(35.2, 45, 0)
$\boldsymbol{B_1}$	{211} <$0\bar{1}1$>	(50.7, 65.9, 63.3)
$\boldsymbol{B_2}$	{121} <$\bar{1}01$>	(129.2, 65.9, 26.5)
$\boldsymbol{C_1}$	{111} <$0\bar{1}1$>	(60, 54.7, 45)
$\boldsymbol{C_2}$	{111} <$\bar{1}01$>	(120, 54.7, 45)
Cu	{001} <100>	(0, 0, 0)
RCu	{011} <$0\bar{1}1$>	(90, 45, 0)

* {hkl}//(TD, ND) plane and <uvw>//RD

3.2.Microstructure and texture of TIMETAL 21S after FSW

Figure 4a shows the wide field orientation map (about 16 x 4 mm^2) of the transversal cross-section of the weld 21S alloy. The AS and RS of the weld sample are identified in the Figure. Basically, the AS and RS regions are created due to the nature of the stirring process [39]. In AS region, the rotation and translation have the same direction which leads to an increase of

plastic deformation and heat in this region. In contrast, the rotation and translation directions are opposite in RS region which results in lower deformation [39].

The microstructure and texture of zones 1 to 7 indicated by black rectangles will be inspected in the next sections. The typical FSW zones SZ and BM can be easily distinguished in Figure 4a. The transition zones (TMAZ and HAZ) between the SZ and BM can be identified with smaller EBSD areas (see next sections). As can be seen, the two sheets are well bonded in the SZ region. The SZ is free of defects and has a basin shape with a notably spreading near the top surface due to the effect of the tool shoulder on material flow during FSW. In addition, the SZ is not symmetric and it is shifted toward RS which is a characteristic of the tool movement on both sides (AS and RS) during the welding.

Even if the deformation in SZ is complicated during the FSW, it is recognized as a simple shear deformation mode [14, 28, 40]. Accordingly, the texture in this zone is a simple shear texture and it is usually presented in the SPN-SD plane where SPN is the shear plane normal and SD is the shear direction [41]. Before going further, it is important to identify the relation between (ND, TD) and (SPN, SD) references frames. In FSW, the shear plane is considered parallel to the pin column surface (SZ/TMAZ border as indicated by dash line in Figures 4b and c) [14, 28, 40]. In this case, the shear plane is not constant within the SZ and follows a curved surface across the SZ due to the rotation of the pin [28, 42]. Based on that, in the center of the SZ (zones 1 to 4), the TD and ND should be parallel to SD and SPN as shown in Figure 4b, respectively. Nevertheless, the plastic deformation in zones 2 and 3 is driven by the conical-shaped tool probe [28] which results in the deviation of SPN from ND. Hence, suitable rotations along TD and WD must be performed to present the texture of zones 2 and 3 in the simple shear (SPN, SD) reference frame. For zone 7, Figure 4c shows that the angle between SPN and ND is around 45° and SD coincide with WD on the AS region since it is well accepted that the SD is tangential to the tool rotation. Thus, to present the texture in the simple shear (SPN, SD) reference frame the texture data of SZ of the zone 7 must be rotated by 45° around WD and then by 90° around ND.

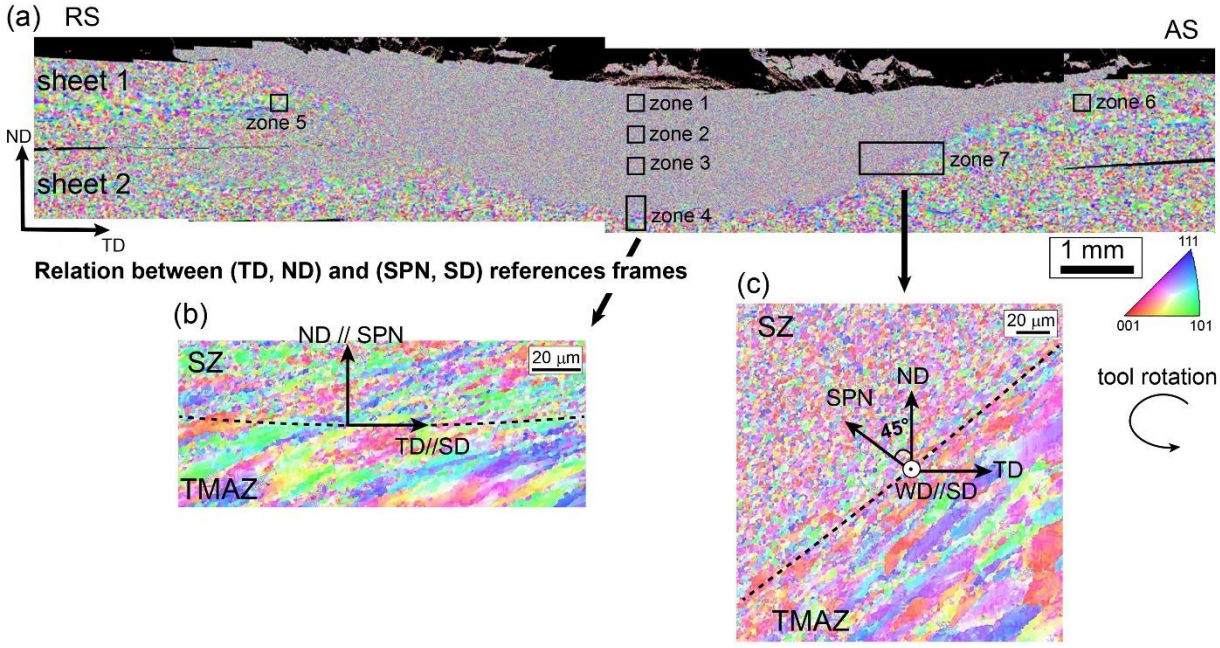

Figure 4: (a) WD-IPF map of the transversal cross-section of the weld 21S alloy, (b, c) relation between (TD, ND) and (SPN, SD) reference frames in the SZ center and SZ near the AS region, respectively.

3.2.1. Microstructure and texture of SZ through thickness

The variation of microstructure through the thickness of SZ is shown in Figure 5a. The black zones in the maps correspond to the areas with CI values lower than 0.05 and may be attributed to distorted nature of the sample due to the high deformation. Excellent grain refinement is occurred in the SZ zone, in which the grain size decreases drastically from 43 µm (BM) to a range of 1.2-1.8 µm. It was reported that the grain size of SZ increases from 2 µm (5.08 mm/s) to 3 µm (0.85 mm/s) with the decrease of welding speed of FSWed S21 alloy [14].

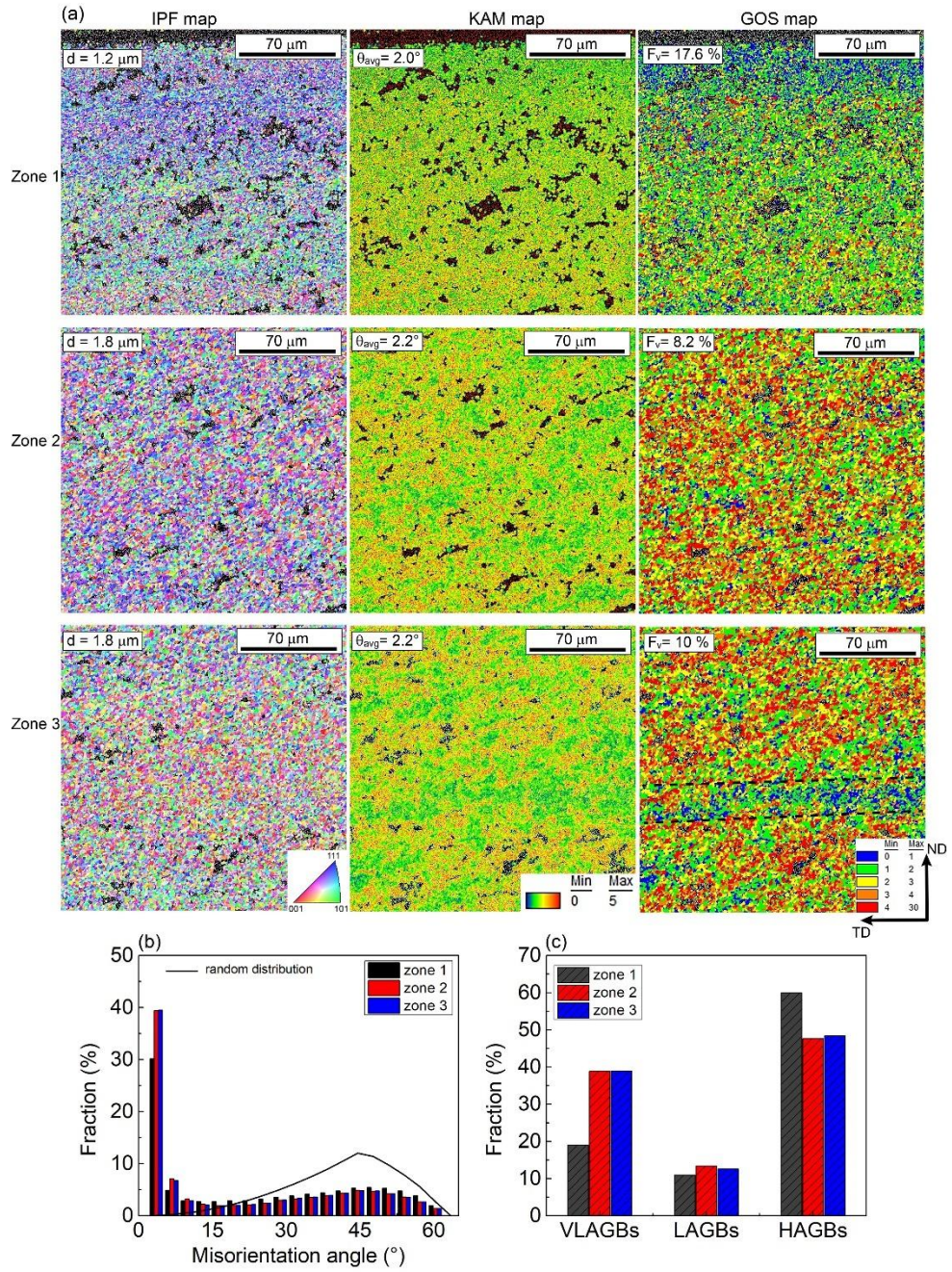

Figure 5: (a) WD-IPF, KAM, and GOS maps, (b) histogram of grain boundary misorientation distribution and (c) evolution of VLAGBs, LAGBs and HAGBs of the zone 1, 2 and 3 in SZ of 21S alloy.

Basically, the microstructure of SZ is similar through thickness except for a higher fraction of recrystallized grains in the top of SZ (zone 1) which can be associated with the stirring effect of the tool shoulder and the possible wear of the welding tool rather than with the temperature gradient. Indeed, several investigations reported that the presence of grain size gradient through the thickness of SZ is caused by the temperature gradient generated from the FSW

tool and the low thermal conductivity of the materials [9-12]. However, the similarity of grain size in the three zones demonstrated that the FSW parameters used for the present study produce low heat input and a small temperature gradient across the thickness. In contrast, Figures 5b and c indicate that this small temperature gradient affects the evolution of grain boundaries type: very low grain boundaries (VLAGB) with misorientation $2° < \theta < 5°$, LAGBs with $5° < \theta < 15°$ and (High) HAGBs with $\theta > 15°$. As can be observed, the three zones contain a similar fraction of LAGBs (~ 12 %). While the microstructure of the top of SZ (zone 1) contains the highest fraction of HAGBs (about 60 %). Zones 2 and 3 are characterized by a high fraction (about 39 %) of VLAGBs indicating a high dislocation density which still not transformed to LAGBs or HAGBs due to low temperature in these zones.

The GOS map indicates the presence of layer structure in zone 3 as shown by the dashed line in Figure 5a. The formation of layer structure in the SZ results from the plastic flow of the transferred metal during welding, which is arising from the tool shoulder and stir pin [7, 11]. The interaction between different layers leads to an inhomogeneous deformation and plastic strains which affect directly the microstructure and texture. As already shown in Figure 5a, the grain refinement is very similar through the SZ thickness. In contrast, a net difference in texture evolution can be noticed through thickness as shown in Figure 6. Zone 1 exhibits a typical shear texture with the presence of all shear texture components except the D_1 component. The ideal shear texture components of BCC materials are shown for comparison in Figure 6 and their description is given in Table 3. The original and rotated {110} pole figures and ODF sections at $\varphi_2 = 45°$ of zone 2 and 3 are shown in Figure 6. The texture of zone 2 seems quite similar to the zone 1. While, the texture of zone 3 shows the domination of D_1, $\bar{J}$, and F texture components. The degradation of the typical shear texture of the SZ zone through the thickness is attributed to the complexity of deformation and strain heterogeneity. The development of texture gradient through SZ thickness could explain the difference in the grain boundary distribution in these zones as shown in Figures 5b and c.

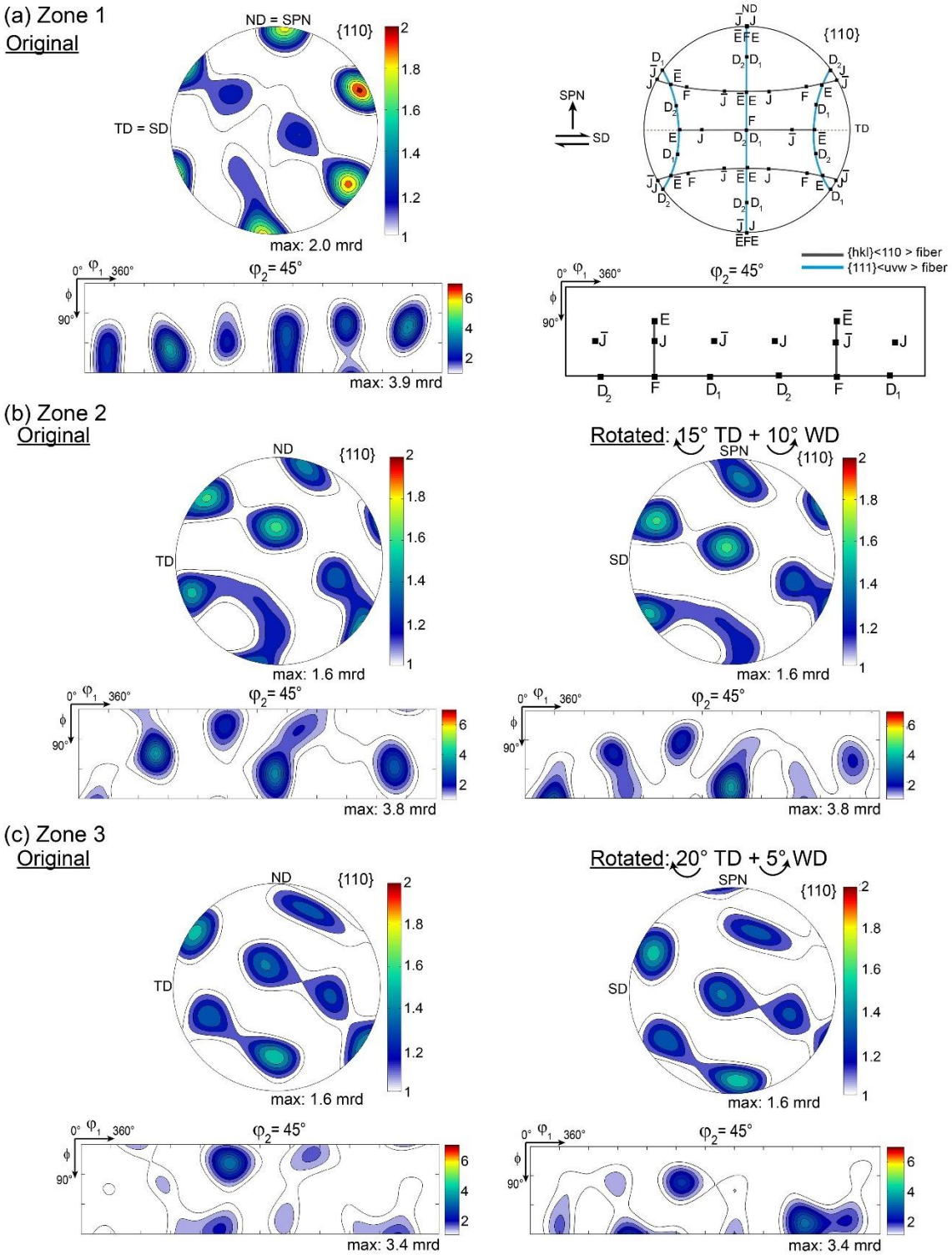

Figure 6: Original and rotated {110} pole figures and ODF sections at φ_2 = 45° of (a) zone 1, (b) zone 2, and (c) zone 3 of SZ of welded 21S alloy. Main ideal shear texture component positions in {110} pole figure and ODF section at φ_2 = 45° of BCC alloys are presented for comparison.

Table 3. Position of ideal shear texture components for BCC materials projected in SPN-SD plane [43].

Notation	**SPN-SD plane**	
Shear component	Miller indice {hkl}<uvw>	Euler angles (°) (φ_1, Φ, φ_2)
$\boldsymbol{D_1}$	{011} <$1\bar{1}1$>	(54.7, 45, 0)
$\boldsymbol{D_2}$	{101} <$\bar{1}11$>	(125.2, 45, 90)
J	{111} <$\bar{1}\bar{1}2$>	(90, 54.7, 45)
$\boldsymbol{\bar{J}}$	{111} <$1\bar{2}1$>	(30, 54.7, 45)
E	{112} <$\bar{1}\bar{1}1$>	(90, 35.2, 45)
$\boldsymbol{\bar{E}}$	{121} <$1\bar{1}1$>	(39.2, 65.9, 26.5)
F	{011} <100>	(0, 45, 0)

3.2.2. Microstructure and texture of zone 4 (SZ, TMAZ and HAZ)

The WD-IPF map of zone 4 shown in Figure 7 enclosed three regions: region 1: SZ, region 2: TMAZ and region 3: HAZ. The WD-IPF and GOS maps, grain size distribution and grain boundaries distribution of the three regions are given at higher magnifications in the same Figure. The mean grain size, HAGBs fraction, mean KAM value and dislocation density of SZ, TMAZ and HAZ regions are summarized in Table 4. The evolution of the texture in the three regions is presented in Figure 8.

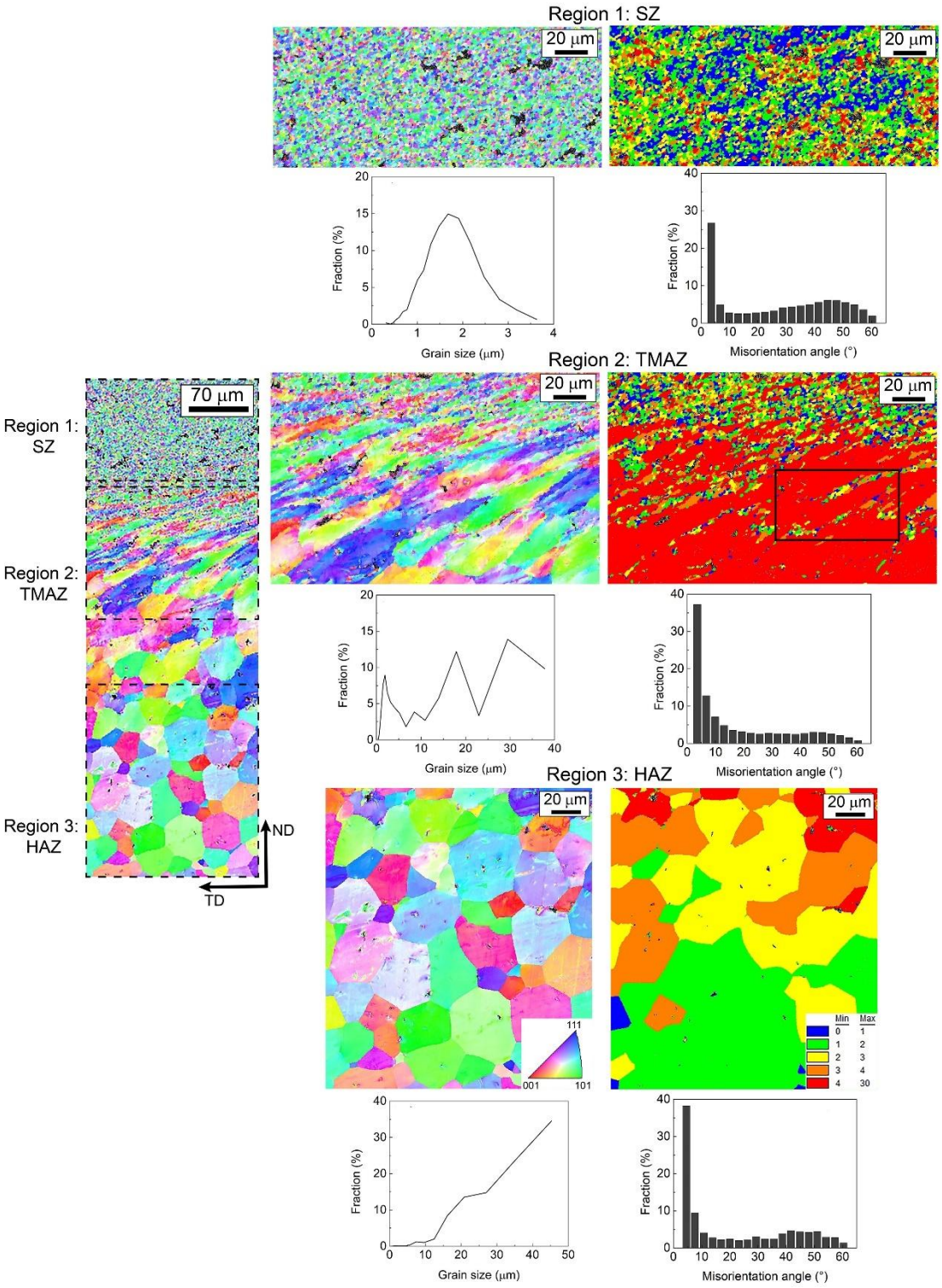

Figure 7: WD-IPF map, GOS map, grain size distribution, misorientation angle distribution of SZ, TMAZ and HAZ regions in zone 4 of FSW 21S alloy, respectively.

Table 4. Mean grain size, HAGBs fraction, mean KAM value and dislocation density of SZ, TMAZ and HAZ region in zone 4 of FSW 21S alloy.

Region	d (μm)	HAGBs (%)	KAM (°)	$\rho \times 10^{14}$ (m^{-2})
SZ	1.6	62.9	1.76	5.48

TMAZ	13.7	34.6	1.86	5.79
HAZ	32.7	45.0	0.88	2.74

Obviously, the different regions of the joint, SZ, TMAZ, and HAZ, exhibit different grain size, grain morphology and texture. As already seen in section 3.2, region 1 which presents the bottom of SZ exhibits an excellent grain refinement (1.6 µm) and typical shear texture with a domination of D_2 component. Several studies reported the domination of D_2 or D_1 components in FSW- BCC materials [5, 14, 28, 29, 44, 45]. It is believed that the domination of grains with D_2 or D_1 texture component is attributed to the activation of {112}<111> slip system [28]. The similarity of microstructure in region 1 with zones 1 to 3 (Figure 5) confirms the uniform grain refinement throughout the SZ thickness.

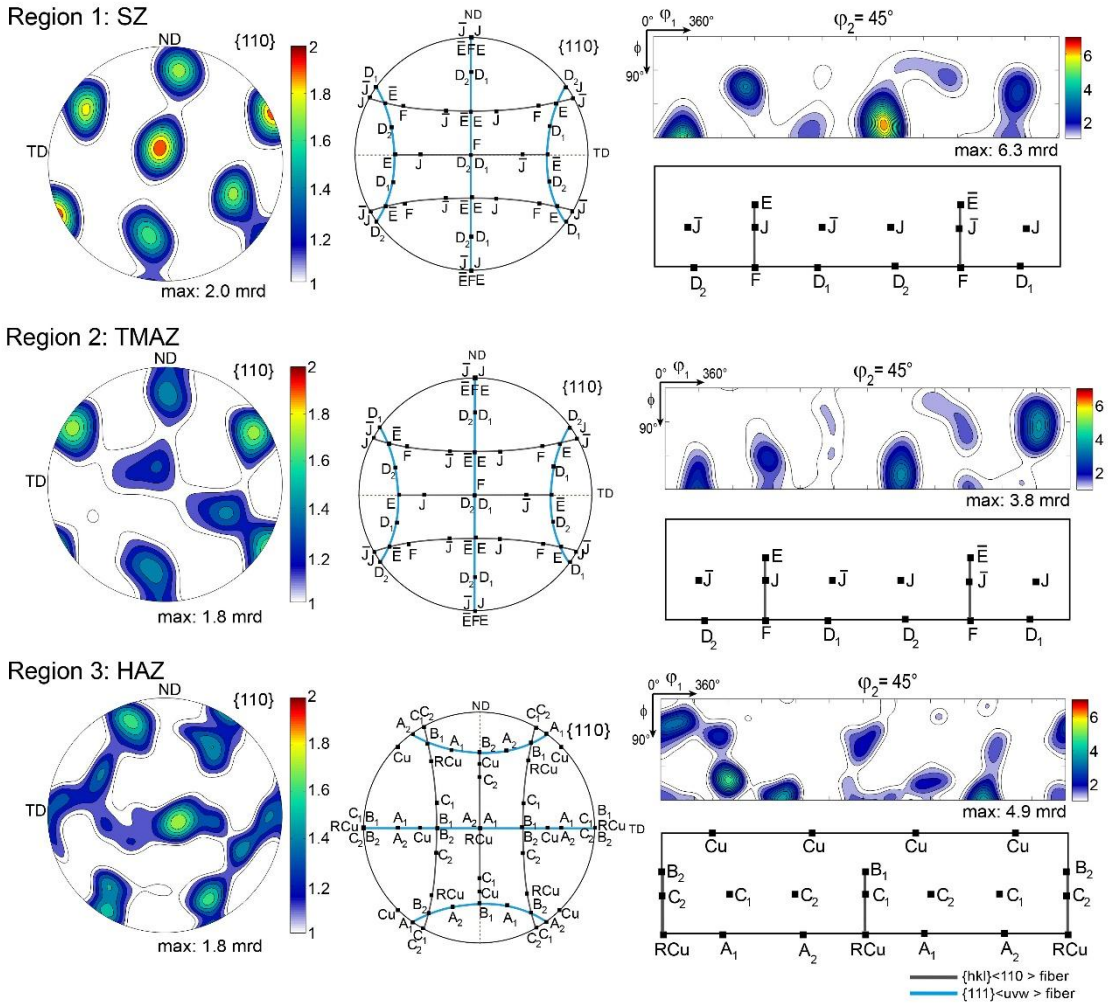

Figure 8: {110} pole figure and ODF section at φ_2 = 45° of region 1 (SZ), region 2 (HAZ), region 3 (BM) of zone 4 of welded 21S alloy. Main ideal BCC texture component positions in {110} pole figure and ODF section at φ_2 = 45° are presented for comparison.

It is known that the grain refinement in FSW material is caused by the occurrence of dynamic recrystallization. This is in good agreement with the present results since the SZ zone shows a higher fraction of recrystallized grains and HAGBs compared to the TMAZ and HAZ zones (see Table 4).

The TMAZ area, which is the transition area between SZ and HAZ, is characterized by a mixture of elongated and equiaxed grains owing to an upward flow of material near the SZ during the operation of plunging and stirring. The dislocation density is higher in this zone which means this zone is highly deformed. It can clearly see from the GOS map of the TMAZ that the elongated grains are surrounded by the small recrystallized grains. The magnification of the rectangle zone in the GOS map (Figure 7) is shown in Figure 9. The serration or the bulging of the original grain boundaries (seen in grain G1) indicates the nucleation of new grains through strain-induced boundary migration (SIBM) mechanism which is ranked as discontinuous dynamic recrystallization (DDRX) [46]. The bulging of the grain boundaries is caused by the difference in dislocation density between the two sides of the grain boundaries [46]. With further strain, the misorientation between the bulges and deformed grains increases, leading to the development of sub-grain boundaries and LAGBs as shown in the grain boundary map (Figure 9b) and then transformed into HAGBs and the bulged regions become DRX grains as can be seen in grain G2 (Figure 9a). It must be noted that grain G3 shows an orientation gradient and contains sub-grain boundaries and LAGBs inside it. This is a characteristic of continuous DRX (CDRX) by sub-grain development (SD) mechanism [46]. In this mechanism, the LAGBs are developed and gradually transformed to HAGBs by the accumulation and continuous absorbing of dislocations inside the deformed grain [46].

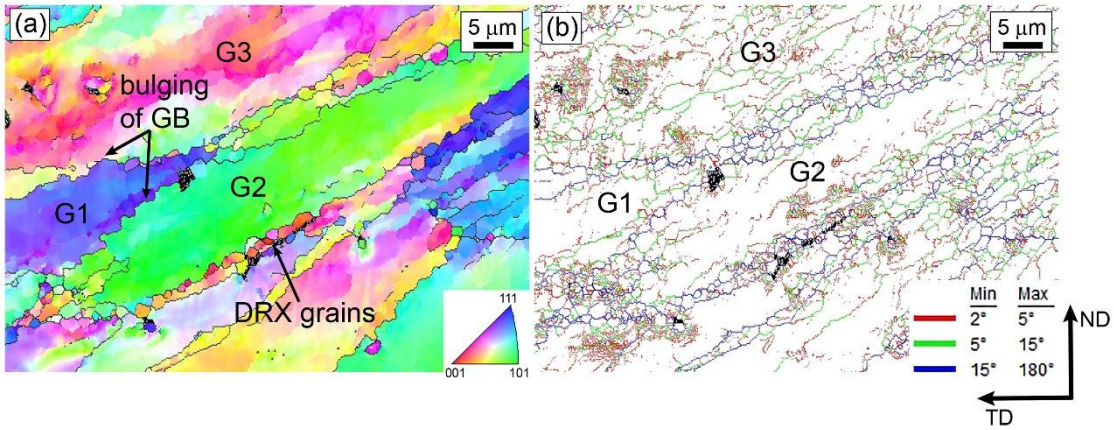

Figure 9: (a) WD-IPF, and (b) grain boundary map: sub-boundaries (1°-5°) highlighted by red lines, LAGB (5–15°) indicated by green lines, and HAGB>15° presented by blue lines.

However, the HAGBs are still not developed at this stage of processing. Similar observation was reported for β-type Ti-15V-3Cr-3Al-3Sn (wt.%) alloy processed by FSW [28]. It is believed that the grain refinement in the SZ is dominated by the CDRX mechanism due to the severe plastic deformation and high temperature in this zone [28].

The microstructure and texture of the HAZ zone are quite similar to the BM except the grain size is smaller and high fraction of deformed grains. It is recognized that the HAZ is only affected by the heat generated during welding which caused the increase of grain size compared to the BM. However, it is not the case in the present investigation. The decrease of grain size and increase of deformation features (Table 4) in HAZ indicated that this zone is also affected by deformation. In fact, this zone is very close to the TMAZ which can be considered as a transition zone between TMAZ and the real HAZ. This could explain the presence of deformation features in this zone.

3.2.3. Microstructural, textural evolution and related strengthening mechanism

The WD-IPF map of zone 7 (indicated in Figure 4) is shown in Figure 10a. The wide field orientation map of this zone allows to visualize the SZ, TMAZ and HAZ in the AS region. The grain size gradient from the SZ to the HAZ is well seen from the WD-IPF map. The texture of area 1 to area 6 is shown in Figure 10b via {110} pole figure.

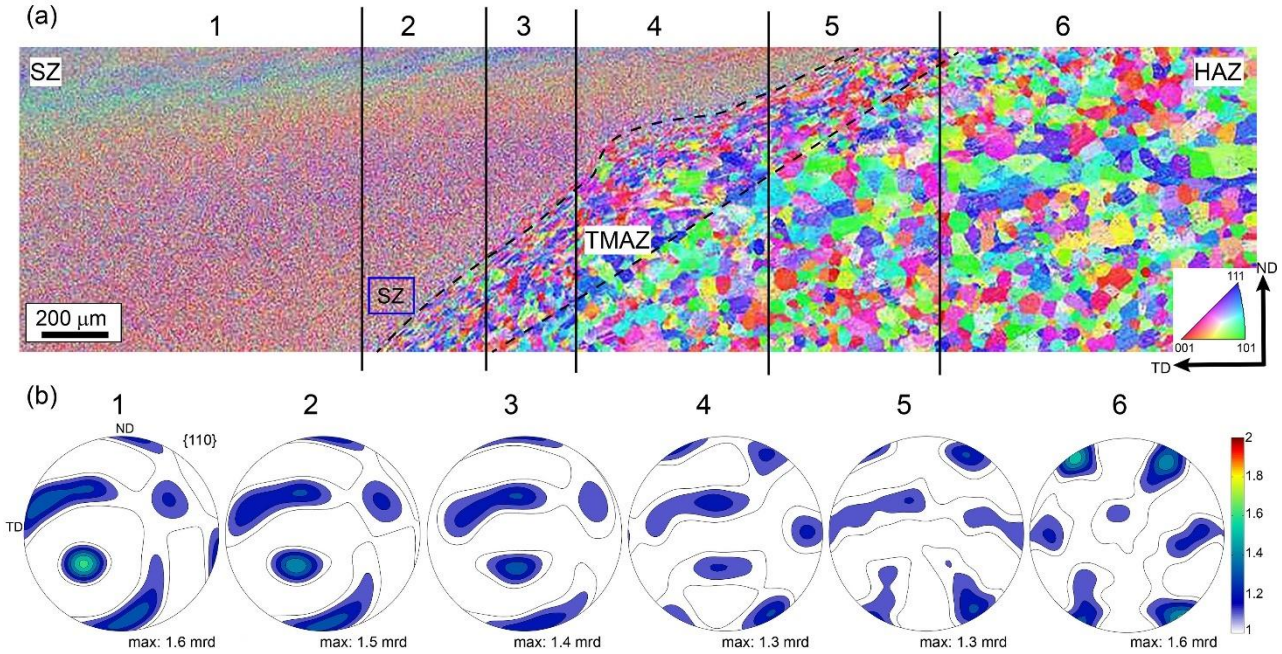

Figure 10: (a) WD-IPF map of zone 7, as indicated in Figure 4 and (b) {110} pole figure corresponding to the 1–6 areas given on the WD-IPF map, respectively.

From the Figure 10b, it can be seen the gradient transformation of initial rolling texture into shear texture through the three zones (HAZ, TMAZ and SZ). As explain in section 3.2, the texture data of SZ must be rotated to be presented in the conventional SPN-SD plane and to have the shear texture component in their correct positions. Examples between the original and suitable rotated pole figures and ODF sections at $\varphi_2 = 45°$ of area 1 and SZ belonging the area 2 (blue box) are shown in Figure 11.

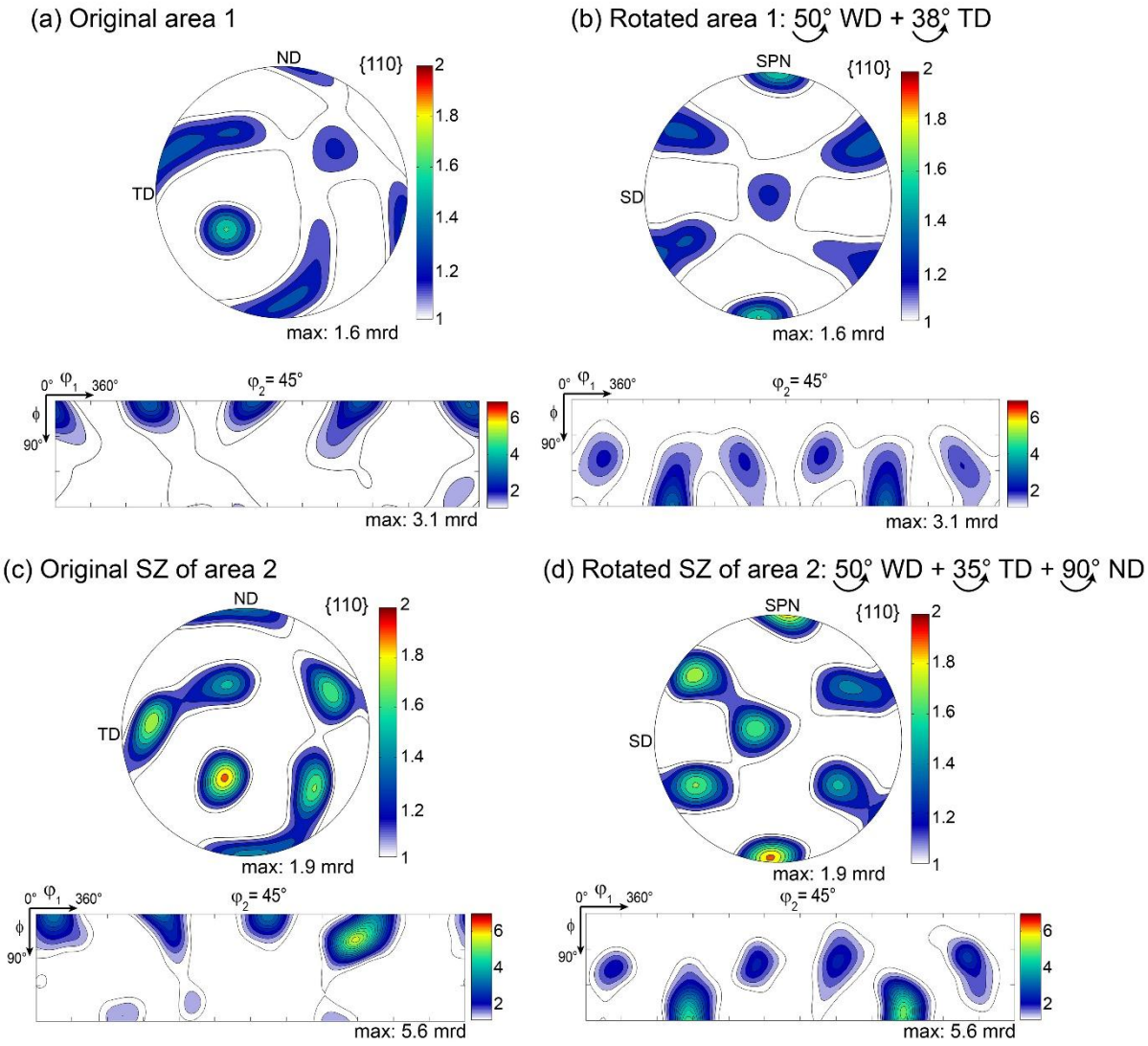

Figure 11: Example between (a) original pole figure and ODF section at φ_2 = 45° and (b) rotated pole figure and ODF to coincide with the SPN-SD plane of area 1 (SZ) and blue box in area 2 shown in Figure 10.

The evolution of microstructural parameters like grain size, dislocation density and grain boundary type (VLAGBs, LAGBs, and HAGBs) and the texture strength within the 6 areas are shown in Figure 12. The grain size (Figure 12a) gradually decreases from HAZ to SZ due to the increase of dislocation density (Figure 12b). However, the dislocation density decreases in SZ due to the occurrence of DRX which results in grain refinement in this zone. The increase of HAGBs and the decrease of VLAGBs (Figure 12c) within these zones are in good agreement with the occurrence of grain refinement mechanism. In contrast, the texture index shown in Figure 12d indicates that the texture strength decreases between HAZ and TMAZ

areas and then increases in the SZ probably because of the transformation of the texture from rolling to shear texture type.

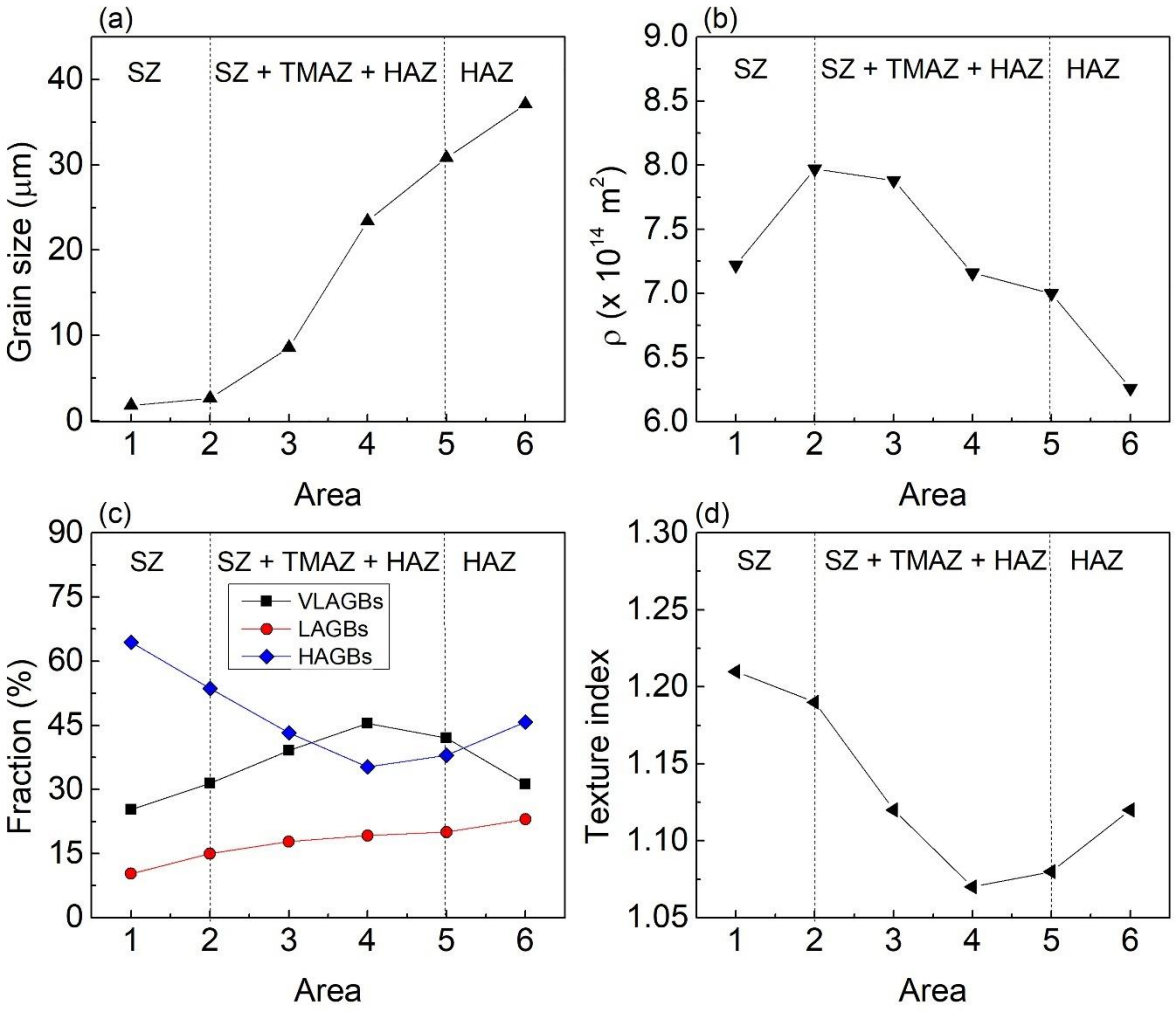

Figure 12: Evolution of (a) grain size, (b) dislocation density, (c) grain boundaries type and (d) texture index within HAZ, TMZ and SZ (1 to 6 areas).

The strengthening, σ, of materials induced by deformation processing is commonly attributed to the grain size strengthening ($\frac{k_{HP}}{\sqrt{d}}$), dislocation strengthening ($\alpha_1 M_R G b \sqrt{\rho}$), and texture strengthening ($\frac{M_T}{M_R}$), following to the equation [43]:

$$\sigma = \frac{M_T}{M_R}\left(\sigma_0 + \alpha_1 M_R G b \sqrt{\rho} + \frac{k_{HP}}{\sqrt{d}}\right) \quad (3)$$

where M_T is the Taylor factor predicted for the deformed material, M_R is the Taylor factor for a random texture, σ_0 is the friction stress, α_1 is a constant, G is the shear modulus and k_{HP} is the Hall–Petch constant.

According to the results shown in Figure 13, it can be suggested that the mechanical properties in HAZ are govern by grain size and dislocation strengthening. The three strengthening mechanisms are responsible for mechanical properties in the TMAZ. While, grain size and texture strengthening mechanisms are dominated in SZ. Obviously, measurements of mechanical properties such as microhardness or tensile test are needed to confirm these speculations.

4. Conclusion

The microstructure and texture evolutions of TIMETAL 21S alloy processed by friction stir lap welding were investigated using EBSD, and the following conclusions were obtained:

- The two TIMETAL 21S sheets were successfully welded by friction stir lap welding.
- According to the microstructural and textural evolution, the weld region of 21S alloy can be separated into four zones: BM, HAZ, TMAZ, and SZ.
- The microstructure of SZ was similar through the thickness and an excellent grain refinement (1.2-1.8 μm) was obtained during the FSLW. In contrast, a shear texture gradient is developed across the thickness due to the complexity of deformation.
- The characteristic of the microstructure of TMAZ demonstrates the occurrence of DDRX. A typical shear texture is developed in this zone.
- The microstructure and texture of HAZ are quite similar to those of BM.
- The concomitant occurrence of grain size, dislocation and texture strengthening is responsible for the mechanical property distribution in different parts of FSLW joint.

Acknowledgements

The authors thank Dr. Y. Millet (TIMET Savoie, Ugine, France) for supplying the TIMETAL 21S sheets. A. Robineau and J.C. Goussain (Institut de Soudure, Goin, France) are gratefully acknowledged for the FSW.

Data availability

The raw/processed data required to reproduce these findings cannot be shared at this time as the data also forms part of an ongoing study.

References

[1] M.K. Besharati Givi, P. Asadi, 1 - General introduction, in: M.K.B. Givi, P. Asadi (Eds.), Advances in Friction-Stir Welding and Processing, Woodhead Publishing, 2014, pp. 1-19.

[2] V.P. Singh, S.K. Patel, A. Ranjan, B. Kuriachen, Recent research progress in solid state friction-stir welding of aluminium–magnesium alloys: a critical review, Journal of Materials Research and Technology 9(3) (2020) 6217-6256.

[3] M.S.M. Isa, K. Moghadasi, M.A. Ariffin, S. Raja, M.R.b. Muhamad, F. Yusof, M.F. Jamaludin, N.b. Yusoff, M.S.b. Ab Karim, Recent research progress in friction stir welding of aluminium and copper dissimilar joint: a review, Journal of Materials Research and Technology 15 (2021) 2735-2780.

[4] K. Singh, G. Singh, H. Singh, Review on friction stir welding of magnesium alloys, Journal of Magnesium and Alloys 6(4) (2018) 399-416.

[5] S. Mironov, Y.S. Sato, H. Kokawa, Microstructural evolution during friction stir-processing of pure iron, Acta Materialia 56(11) (2008) 2602-2614.

[6] K. Gangwar, M. Ramulu, Friction stir welding of titanium alloys: A review, Materials & Design 141 (2018) 230-255.

[7] K. Kumar, S.V. Kailas, The role of friction stir welding tool on material flow and weld formation, Materials Science and Engineering: A 485(1) (2008) 367-374.

[8] R.S. Mishra, Z.Y. Ma, Friction stir welding and processing, Materials Science and Engineering: R: Reports 50(1) (2005) 1-78.

[9] S. Yoon, R. Ueji, H. Fujii, Effect of rotation rate on microstructure and texture evolution during friction stir welding of Ti–6Al–4V plates, Materials Characterization 106 (2015) 352-358.

[10] S. Yoon, R. Ueji, H. Fujii, Microstructure and texture distribution of Ti–6Al–4V alloy joints friction stir welded below β-transus temperature, Journal of Materials Processing Technology 229 (2016) 390-397.

[11] W. Han, P. Liu, X. Yi, Q. Zhan, F. Wan, K. Yabuuchi, H. Serizawa, A. Kimura, Impact of friction stir welding on recrystallization of oxide dispersion strengthened ferritic steel, Journal of Materials Science & Technology 34(1) (2018) 209-213.

[12] M.M.Z. Ahmed, B.P. Wynne, W.M. Rainforth, A. Addison, J.P. Martin, P.L. Threadgill, Effect of Tool Geometry and Heat Input on the Hardness, Grain Structure, and Crystallographic Texture of Thick-Section Friction Stir-Welded Aluminium, Metallurgical and Materials Transactions A 50(1) (2019) 271-284.

[13] Z.Y. Ma, F.C. Liu, R.S. Mishra, Superplastic deformation mechanism of an ultrafine-grained aluminum alloy produced by friction stir processing, Acta Materialia 58(14) (2010) 4693-4704.
[14] A.P. Reynolds, E. Hood, W. Tang, Texture in friction stir welds of Timetal 21S, Scripta Materialia 52(6) (2005) 491-494.
[15] J. Zhang, X. Chen, D. Xia, G. Huang, A. Tang, B. Jiang, F. Pan, Improving performance of friction stir welded AZ31/AM60 dissimilar joint by adjusting texture distribution and microstructure, Materials Science and Engineering: A 778 (2020) 139088.
[16] R. Kumar, A. Nait Salah, N. Kant, P. Singh, A.W. Hashmi, C. Malla, Effect of FSW process parameters on mechanical properties and microstructure of dissimilar welded joints of AA2024 and AA6082, Materials Today: Proceedings 50 (2022) 1435-1441.
[17] S. Mironov, Y. Zhang, Y.S. Sato, H. Kokawa, Development of grain structure in β-phase field during friction stir welding of Ti–6Al–4V alloy, Scripta Materialia 59(1) (2008) 27-30.
[18] P. Edwards, M. Ramulu, Effect of process conditions on superplastic forming behaviour in Ti–6Al–4V friction stir welds, Science and Technology of Welding and Joining 14(7) (2009) 669-680.
[19] H.J. Liu, L. Zhou, Q.W. Liu, Microstructural characteristics and mechanical properties of friction stir welded joints of Ti–6Al–4V titanium alloy, Materials & Design 31(3) (2010) 1650-1655.
[20] L.H. Wu, B.L. Xiao, D.R. Ni, Z.Y. Ma, X.H. Li, M.J. Fu, Y.S. Zeng, Achieving superior superplasticity from lamellar microstructure of a nugget in a friction-stir-welded Ti–6Al–4V joint, Scripta Materialia 98 (2015) 44-47.
[21] S. Yoon, R. Ueji, H. Fujii, Effect of initial microstructure on Ti–6Al–4V joint by friction stir welding, Materials & Design 88 (2015) 1269-1276.
[22] P.D. Edwards, M. Ramulu, Material flow during friction stir welding of Ti-6Al-4V, Journal of Materials Processing Technology 218 (2015) 107-115.
[23] J.-D. Kim, S.P. Murugan, J.W. Kim, C.-K. Chun, S.W. Kim, J.-K. Hong, S.-W. Choi, C. Ji, J.-U. Kim, Y.-D. Park, α/β phase transformation and dynamic recrystallization induced microstructure development in fine-grained Ti-6Al-4V friction stir weld, Materials Characterization 178 (2021) 111300.
[24] C.L. Jia, L.H. Wu, P. Xue, H. Zhang, D.R. Ni, B.L. Xiao, Z.Y. Ma, Effect of static spheroidization on superplasticity of fine lamellae in nugget of a friction stir welded Ti-6Al-4V joint, Journal of Materials Science & Technology (2022).
[25] R.R. Boyer, Aerospace applications of beta titanium alloys, JOM 46(7) (1994) 20-23.

[26] D. Banerjee, J.C. Williams, Perspectives on Titanium Science and Technology, Acta Materialia 61(3) (2013) 844-879.
[27] J.D. Cotton, R.D. Briggs, R.R. Boyer, S. Tamirisakandala, P. Russo, N. Shchetnikov, J.C. Fanning, State of the Art in Beta Titanium Alloys for Airframe Applications, JOM 67(6) (2015) 1281-1303.
[28] H. Liu, H. Fujii, Microstructural and mechanical properties of a beta-type titanium alloy joint fabricated by friction stir welding, Materials Science and Engineering: A 711 (2018) 140-148.
[29] H. Liu, K. Ushioda, H. Fujii, Elucidation of microstructural evolution of beta-type titanium alloy joint during friction stir welding using liquid CO2 cooling, Materials Characterization 145 (2018) 490-500.
[30] Y. Mikami, K. Oda, M. Kamaya, M. Mochizuki, Effect of reference point selection on microscopic stress measurement using EBSD, Materials Science and Engineering: A 647 (2015) 256-264.
[31] J.-H. Cho, A.D. Rollett, K.H. Oh, Determination of a mean orientation in electron backscatter diffraction measurements, Metallurgical and Materials Transactions A 36(12) (2005) 3427-3438.
[32] Y. Ateba Betanda, A.-L. Helbert, F. Brisset, M.-H. Mathon, T. Waeckerlé, T. Baudin, Measurement of stored energy in Fe–48%Ni alloys strongly cold-rolled using three approaches: Neutron diffraction, Dillamore and KAM approaches, Materials Science and Engineering: A 614 (2014) 193-198.
[33] R. Badji, T. Chauveau, B. Bacroix, Texture, misorientation and mechanical anisotropy in a deformed dual phase stainless steel weld joint, Mater. Sci. Eng. A 575 (2013) 94-103.
[34] H. Azzeddine, Y.I. Bourezg, A.Y. Khereddine, T. Baudin, A.-L. Helbert, F. Brisset, M. Kawasaki, D. Bradai, T.G. Langdon, An investigation of the stored energy and thermal stability in a Cu–Ni–Si alloy processed by high-pressure torsion, Philosophical Magazine 100(6) (2020) 688-712.
[35] P. Castany, M. Besse, T. Gloriant, In situ TEM study of dislocation slip in a metastable β titanium alloy, Scripta Materialia 66(6) (2012) 371-373.
[36] F. Bachmann, R. Hielscher, H. Schaeben, Texture Analysis with MTEX – Free and Open Source Software Toolbox, Solid State Phenomena 160 (2010) 63-68.
[37] U.F. Kocks, C.N. Tomé, H.R. Wenk, A.J. Beaudoin, H. Mecking, Texture and Anisotropy: Preferred Orientations in Polycrystals and Their Effect on Materials Properties, Cambridge University Press, 1998.

[38] M. Hölscher, D. Raabe, K. Lücke, Rolling and recrystallization textures of bcc steels, Steel Research 62(12) (1991) 567-575.
[39] R. Nandan, T. DebRoy, H.K.D.H. Bhadeshia, Recent advances in friction-stir welding – Process, weldment structure and properties, Progress in Materials Science 53(6) (2008) 980-1023.
[40] S.H.C. Park, Y.S. Sato, H. Kokawa, Basal plane texture and flow pattern in friction stir weld of a magnesium alloy, Metallurgical and Materials Transactions A 34(4) (2003) 987-994.
[41] S. Li, I.J. Beyerlein, M.A.M. Bourke, Texture formation during equal channel angular extrusion of fcc and bcc materials: comparison with simple shear, Materials Science and Engineering: A 394(1) (2005) 66-77.
[42] S. Mironov, Y.S. Sato, H. Kokawa, Development of grain structure during friction stir welding of pure titanium, Acta Materialia 57(15) (2009) 4519-4528.
[43] H. Azzeddine, D. Bradai, T. Baudin, T.G. Langdon, Texture evolution in high-pressure torsion processing, Progress in Materials Science 125 (2022) 100886.
[44] R.W. Fonda, K.E. Knipling, A.L. Pilchak, Thermal Stir Welds in Titanium, Metallurgical and Materials Transactions A 47(1) (2016) 360-367.
[45] S. Rahimi, B.P. Wynne, T.N. Baker, Development of Microstructure and Crystallographic Texture in a Double-Sided Friction Stir Welded Microalloyed Steel, Metallurgical and Materials Transactions A 48(1) (2017) 362-378.
[46] T. Sakai, A. Belyakov, R. Kaibyshev, H. Miura, J.J. Jonas, Dynamic and post-dynamic recrystallization under hot, cold and severe plastic deformation conditions, Progress in Materials Science 60 (2014) 130-207.